Received: 23 May 2022 | Revised: 8 July 2022 | Accepted: 13 July 2022

DOI: 10.1002/eom2.12264

RESEARCH ARTICLE

EcoMat FUNCTIONAL MATERIALS FOR GREEN ENERGY AND ENVIRONMENT WILEY

Superior cycle performance of Li metal electrode with {110} surface texturing

Xitao Hu[1] | Yao Gao[2] | Biao Zhang[2] | Le Shi[3] | Quan Li[1]

[1]Department of Physics, The Chinese University of Hong Kong, Shatin, Hong Kong. China

[2]Department of Applied Physics, The Hong Kong Polytechnic University, Kowloon, Hong Kong. China

[3]State Key Laboratory of Electrical Insulation and Power Equipment, Center of Nanomaterials for Renewable Energy, School of Electrical Engineering, Xi'an Jiaotong University, Xi'an, China

Correspondence
Le Shi, State Key Laboratory of Electrical Insulation and Power Equipment, Center of Nanomaterials for Renewable Energy, School of Electrical Engineering, Xi'an Jiaotong University, Xi'an 710049, China.
Quan Li, Department of Physics, The Chinese University of Hong Kong, Shatin, New Territories, Hong Kong. China.
Email: le.shi@mail.xjtu.edu.cn and liquan@cuhk.edu.hk

Funding information
CUHK

Abstract

Li metal foil is a most promising candidate for Li metal batteries, but its poor cycle stability remains a major obstacle limiting its development for practical applications. In the present work, we show that crystallographic orientation (surface texturing) of Li foil plays a key role in determining the cycle performance of the Li metal anode in both symmetrical cells and full cells. Li foil of {110} texturing is demonstrated to have superior cycling stability when compared to Li {100} or pristine Li foils without specific texturing. Experimental evidence and computational modeling suggest that the enhanced cycle performance of Li {110} originates from the low-surface energy/surface diffusion barrier associated with the Li {110} plane, leading to not only dense Li plating but also uniform stripping during cycling. Capacity retention of 96.1% (125.0 mAh/g) after 400 cycles is demonstrated in a full cell with Li {110} anode and $LiFePO_4$ cathode at 1 C. This work adds to the current understanding of electrochemical plating/stripping of Li metal, and leads to new technologies that can largely extend the cycle life of Li metal electrode for the next generation of energy storage devices.

KEYWORDS

energy conversion and storage, green technology, sustainability

1 | INTRODUCTION

Lithium metal, a promising anode material for Li-based energy storage devices, has high-energy density (3861 mAh/g) and the lowest electrode potential (−3.04 V vs. SHE) among all anode candidates. However, a most fundamental problem of Li-metal anode that limits its practical application is the poor cycle performance of the anode due to the uncontrollable Li plating/stripping process.[1] The Li growth kinetics as well as the inhomogeneity at the electrode surface promotes the dendrite growth.[2] The loose structure of the formed dendrites makes them easily break off from the electrode, causing "dead lithium"; while the fractured Li surfaces would continuously react with the electrolyte, consuming both Li and the electrolyte. Both processes result in a low Columbic efficiency and reduced cycle life. In addition, the sharp dendrites could pierce the battery separator and result in internal short-circuit, which may induce thermal runaway in batteries, imposing serious safety concerns.

Many strategies have been developed to improve the cycle performance of the Li-based electrode. Methods include mechanically blocking the growth of lithium dendrites by using capping materials of high-shear modulus[3–5];

improving the Li nucleation uniformity by manipulating the architecture of current collector, and modifying the anode surface or solid electrolyte interphases[6–8]; as well as restricting the uneven Li growth by forming a high surface energy capping.[9,10] Although these methods indeed suppress the Li dendrite growth to a certain extent, the problem persists and remains a major obstacle limiting the cycle performance of Li metal anode.

A largely unexplored aspect is the effect of pristine Li texturing on Li plating/stripping characteristics and eventually the cycle performance of the electrode. Here texturing refers to the preferential crystallographic orientation, instead of that commonly used in tribology (i.e., specific surface topographical features resulted from the engineering process).[11] Generally speaking, different crystalline planes associate with different surface energies and surface diffusion energy barriers, and thus affect the nucleation and growth of Li in a battery process. As a matter of fact, {0001} texturing of Zn foils has been found to be beneficial for the long cycle performance of Zn-based batteries.[12–14] Some earlier experimental results suggested that similar principles may apply to the Li-metal electrode. Cui's group was the first to report Li growing into a {110} texturing in specific electrolytes in 2017, and such a textured growth indeed associated with smooth termination surfaces.[15] The same group also found the slow growth of Li along <110> crystalline direction when studying the Li nanowire growth using electron microscopy.[16] Gu et al. inferred from simulation results that the growth of Li on Cu {100} preferred to be along the <110> Li crystalline direction, and the Li plated on Cu {100} indeed showed prolonged cycle life.[17] Most recently, Zhao et al. demonstrated the formation of {110} texturing in Li films electroplated on Cu foil. When employed as the electrode with ether electrolyte, a 2500 min' cycle life at a current density of 1 mA/cm^2 is shown in a symmetrical cell.[18] Compared to Cu anode, the direct usage of Li foil as the anode does not require any pre-lithiation process in batteries of Li-free cathode, and thus is of great interest. Recently, preparation of Li {100} texturing was realized by severe plastic deformation upon cold rolling of Li foil.[12] However, the prepared Li foil with {100} texturing did not show significantly improved electrochemical performance when used as the electrode.[12] As a matter of fact, the Li {100} plane was suggested to have the lowest surface energy in vacuum in early literatures.[19,20] Nevertheless, a more recent theoretical study shows that Li {110} plane associated with the lowest surface energy and surface diffusion barrier in a practical battery working range.[21] However, Li foil with {110} texturing is not available to date, and whether such texturing can enhance the cycle performance of the electrode remains unclear.

In the present work, we show that both {110} and {100} texturing can be prepared for Li metal foil with simple mechanical methods. Electrode made of Li metal foil of {110} texturing significantly outperforms that made of Li foil of {100} texturing as well as the pristine Li foil (no specific texturing). The enhanced cycle performance of Li foil with {110} texturing is ascribed to the uniform Li stripping from /dense plating on the Li foil of {110} texturing, which features are absent in Li {100} or pristine Li foils. The Li {110} texturing and the flat/dense surface morphology is found to be well maintained upon long cycles, leading to stable cycle performance of the electrode in both symmetrical and full cells. By combing it with other existing strategies, controllable texturing of metal foils will open up new revenue in the field of alkaline metal batteries as it directly affects the plating/stripping behavior of the metal and is also expected to impact the solid electrolyte interphase formation.

2 | RESULTS

2.1 | Formation of preferential surface texturing on Li foils

Li foils of specific surface texturing ({110} and {100} in the present work) can be obtained using mechanical methods (see Section 4 for details), an illustration of which is shown in Figure 1A. Li foils of {100} surface texturing result from a unidirectional pressure exerted on pristine Li foils (a standard sample is a round foil with a diameter of 16 mm and thickness of 600 μm) at room temperature. Such process leads to a ~200 μm Li foil with ~50 μm thick (thickness determination see Figure S1a) {100} surface texturing (Figure 1B) that is stable for at least 30 days (Figure 1B) when being stored in a glove box at room temperature. Generation of Li {110} surface texturing is slightly more complex, when pre-rolling and scraping of pristine Li foil (the same standard starting material) are carried out at room temperature before a further rolling at 75°C. The resulted {110} surface texturing is found to be ~100 μm (Figure S1b) for Li foil of ~200 μm thickness, and it also remains stable for at least 30 days when being stored in a glove box at room temperature (Figure 1C). As shown in the x-ray diffraction (XRD) taken from respective samples, dominant intensities of (200) and (110) diffractions are found in Li {100}, and Li {110} foils, respectively (Figure 1B, C). In contrast, no preferential surface texturing is identified in the starting pristine Li foil samples—while all diffraction peaks can be indexed to the body centered cubic (BCC) Li (JCPDF #15-0401), the intensity ratios of different diffraction peaks vary largely in different pristine Li foil samples examined (three examples shown in Figure S2), suggesting

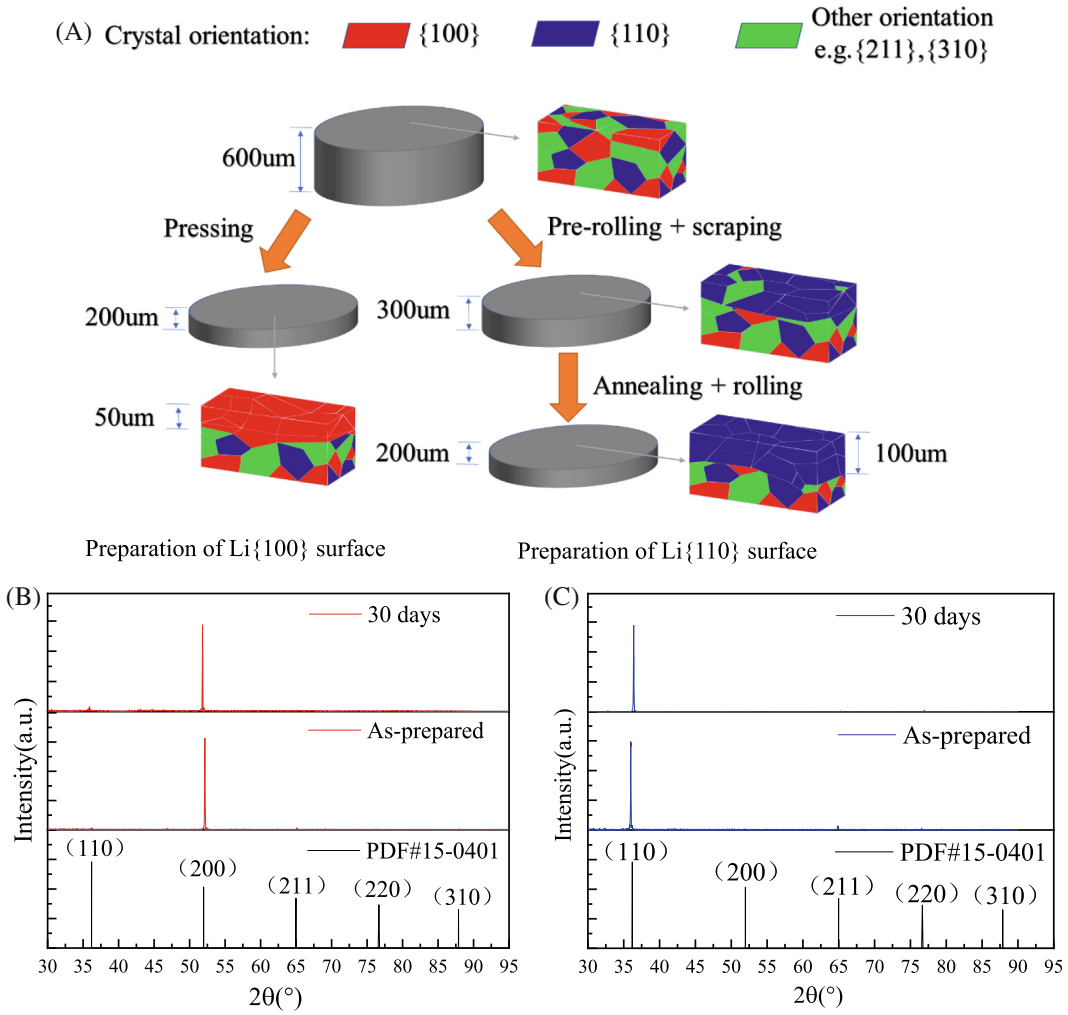

FIGURE 1 (A) Schematic illustration of Li {110} and Li {100} preparation. The XRD of the Li foil with (B) {100} and (C) {110} preferential texturing

a combination of different surface crystallographic orientations.

The formation of texturing on Li foil is mainly driven by the stress induced activation of sliding systems in BCC metals.[22] The most easily activated slip system in BCC metals is {110} <111>, the activation of which promotes the prevalence of cubic texture of {100} <110> in BCC metals under moderate stress, such as those induced by pressing or cold-rolling.[22] The experimental observation of {100} surface texturing formation on Li foil in the present work is consistent with the theory.[23] At higher stress levels, other slip systems in BCC would also be activated, leading to competition among different texture formation.[22] Another common texture in BCC is the shear texture {110} <100>, which occurs when the sample is subjected to shear stress.[24] The pre-rolling and scraping in the present work serve this purpose in preparing the Li foil of {110} surface texturing. However, shear stress itself would not guarantee the dominance of the {110} texturing. Fortunately, it is known that grains of the shear texture bear rather low defect density/stress levels,[25] and such grain would become the core of re-crystallization upon post-annealing, eventually leading to the dominance of {110} texturing in the Li foil. In this regard, the last procedure of mechanical rolling at 75°C is also important, as the elevated temperature drives the proper recrystallization process that leads to the dominance of {110} surface texturing in Li foil. Optimization of the crystallization temperature can be found in the Figure S3. The gentle rolling flattens the surface of the Li foil (effect of each step on the texturing formation can be found in Figure S4).

2.2 | Surface characteristics of pristine Li foil, Li {100}, and Li {110}

To ensure consistent surface chemistry and flatness of the Li metal electrode, chemical polishing of all Li foil

samples was employed before cell assembly. The chemical polishing of all Li foils results in similar flatness (Figure S5a–c) and chemical composition (Figure S5d–g) of the foil surfaces. The sizes of the grains in all samples were found similar, in the range of a few hundreds of microns (Figure S6). To better understand the sample surface composition, X-ray photoelectron spectra (XPS) were taken from all Li samples (Li {110}, Li {100}, and pristine Li foils) before their assembly into cells. Similar surface composition is obtained for all samples examined. The Li 1s spectra (Figure S7a) suggested the presence of Li_2O (binding energy at ~53.6 eV) and Li_2CO_3 (binding energy at ~55.4 eV).[26] Consistent observation was made for the C 1s (Figure S7b), in which the 288.8 eV component originated from Li_2CO_3.[27] Three other peaks fitted at ~287.0, ~285.0, and ~284.6 eV can be assigned to C═O, C—O, and C—H,[28–30] likely coming from the organic contaminations on the foil surface.[31] The O 1s spectra (Figure S7c) can be fitted by four peaks, the one at ~531.8 eV is assigned to Li_2CO_3 and the one at ~528.0 eV to Li_2O.[32,33] The rest two peaks at ~531.4 and ~533.6 eV are ascribed to C═O and C—O, respectively, being common in organic contaminants on the surface of the Li foil.[31]

2.3 | Electrochemical performance of pristine Li foil, Li {100}, and Li {110} electrode

Using such a chemically polished Li foil as the electrode, symmetrical cells were assembled for the electrochemical tests. For pristine Li foil electrode, we plotted the voltage profile of the cell as a function of time (sample b in Figure S8) at a current density of 1 mA/cm^2 and with a capacity of 1 mAh/cm^2. A large fluctuation of the over-potential is observed at the start of the cycling, commonly ascribed to the formation of SEI.[34] After that, the over-potential stabilizes at about 0.15 V. A sudden surge of over-potential occurs at the 99th cycle, together with frequent voltage fluctuations. This is a common indicator of device failure, to which the Li dendrite growth and the formation of dead lithium are known to be major contributors.[35] On the other hand, it is interesting to note that the cycle performance of different Li foils (pristine samples with identical chemical polishing) varies significantly. The drastic increase of over-potential may show after 50 cycles in a "short life" case (sample c in Figure S8), or appear after 200 cycles in a "long life" case (sample a in Figure S8) in samples tested in the present work. The range of cycle life is consistent with the literature.[31,36–38]

To investigate the galvanostatic charge/discharge performances of Li {110} and Li {100}, symmetric cells were assembled and tested at a capacity of 1 mAh/cm^2 and different current densities of 1 and 5 mA/cm^2 in carbonate electrolyte (1.0 M $LiPF_6$ in EC/DEC [v/v = 1:1]). At the current density of 1 mA/cm^2, the voltage hysteresis of both Li {110} and Li {100} remain stable until 250 cycles (Figure 2A). After that, the voltage hysteresis of Li {100} increased rapidly from 180 mV (at 250th cycle) to 323 mV (at 350th cycle), and fluctuation of the voltage profile appeared after ~350 cycles (marked by an arrow in Figure 2A). In contrast, from the 1st cycle to the 400th cycle, voltage hysteresis of Li {110} slowly increased from 141 to 203 mV without much fluctuation. When the current density was increased to 5 mA/cm^2 with a capacity of 1 mAh/cm^2, voltage fluctuation appeared after about 100 cycles and short circuit occurred after about 120 cycles for Li {100} (Figure 2B). In contrast, Li {110} was stable for more than 150 cycles. When capacity was increased to 5 mAh/cm^2 at the current density of 1 mA/cm^2, Li {110} (60 cycles) consistently shown a significantly better performance than those of Li {100} (35 cycles) and pristine Li foil (25 cycles) (Figure S9). The electrochemical behavior of Li {100} or {110} electrode was quite consistent for all samples examined.

More significant voltage hysteresis was always found in Li {100} (vs. Li {110}) at low-current densities of 1 mA/cm^2. At a higher current density of 5 mA/cm^2, the voltage hysteresis of Li {100} and Li {110} was found similar in the first 65 cycles, suggesting that the occurrence of increased ion flow inhomogeneity and aggravated side effects[39,40] started to override the benefit brought by the Li {110} surface. Nonetheless, a longer cycle life was still achieved in the case of Li {110}. Although no artificial SEI is introduced and a most common electrolyte (carbonate without special additive) is employed in the present work, the Li symmetric cell using the Li {110} demonstrated comparable performance to those with artificial SEI (e.g., LiDFOB and graphite fluoride, etc.) in the literature.[41,42] A comparison with the literature can be found in Table S1.

To further evaluate the performance of symmetric cells with Li foils of different texturing, the exchange charge resistance and the exchange current density were investigated by electrochemical impedance spectroscopy (EIS) and Tafel kinetics, respectively. Bulk resistance (R_s), charge transfer (R_{ct}) and SEI (R_{SEI}) resistances can be estimated by fitting the EIS data (Figure 2C, and Figure S10a,b). Charge transfer and SEI resistance represent the capability of charge transfer in the electrode and at the electrode/electrolyte interface. All electrodes show similar bulk resistance (R_s), which does not change much along with cycling (~2.5 Ω at 1st cycle and ~4.8 Ω at 50th cycle). At a current density of 1 mA/cm^2 and with a capacity of 1 mAh/cm^2, both the SEI (R_{SEI}) and the

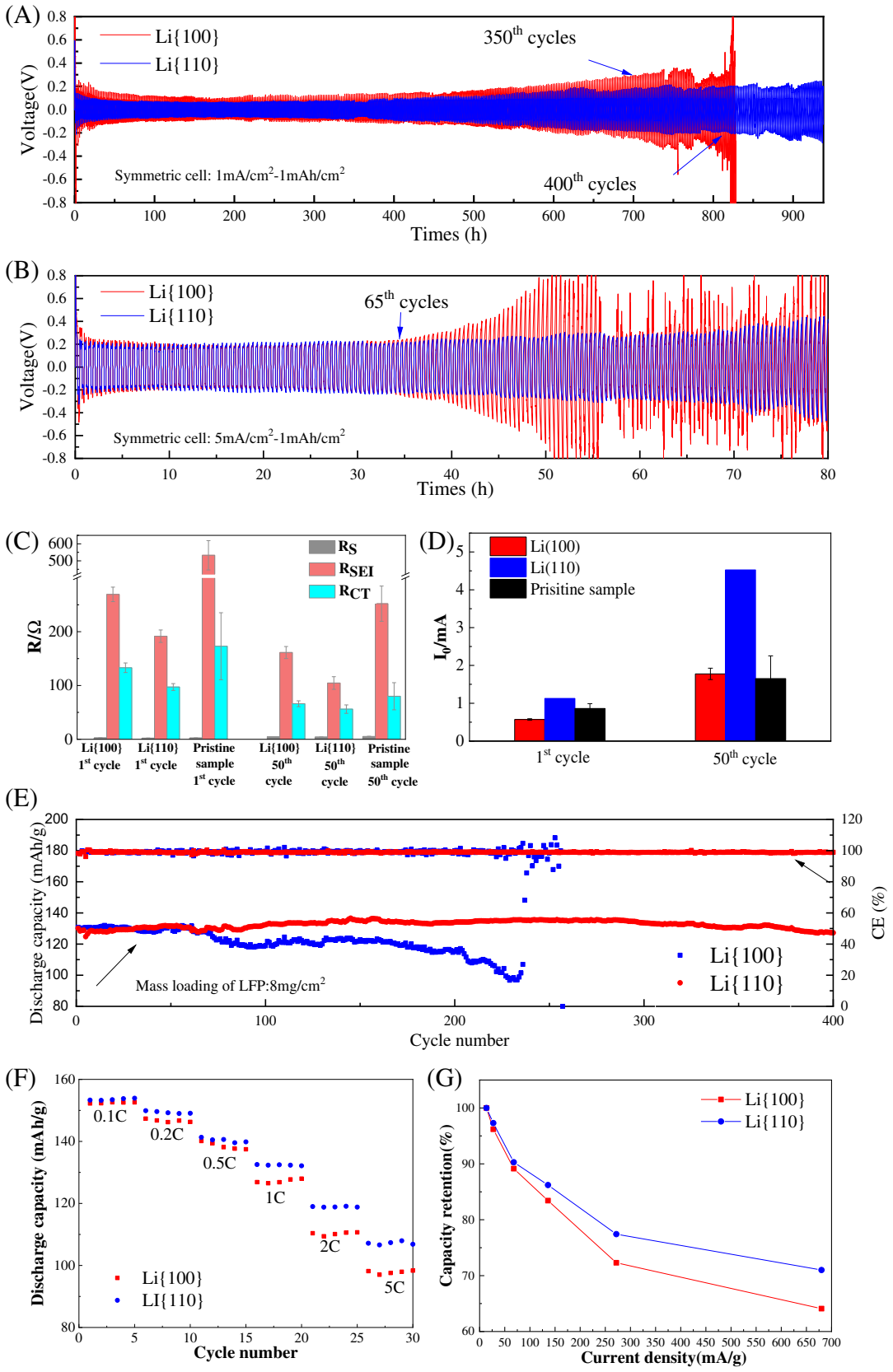

FIGURE 2 Li {100} (red) and Li {110} (blue) symmetric cells at different current densities of (A) 1 mA/cm^2 and (B) 5 mA/cm^2 with a capacity of 1mAh/cm^2. $LiPF_6$/EC-DEC electrolyte was adopted without additive. (C) Bulk resistance (R_s), charge transfer (R_{ct}) and SEI (R_{SEI}) resistances estimated by fitting the corresponding EIS data. (D) Exchange current density comparison among the pristine Li, Li {110}, and Li {100} foils. Electrochemical performances of Li//LFP full cells. (E) Cycling performances of the full cells with Li {100} and {110} anode with LFP mass loading of 8.0 mg/cm^2 at 1 C. (F) Rate capability and (G) capacity retention of the Li//LFP full cells with Li {100} and {110} anode

charge transfer (R_{ct}) resistance of the Li {110} electrode were found to be lower than those of Li {100} (191.6 Ω vs. 269.4 Ω for R_{SEI} and 97.2 Ω vs.133 Ω for R_{ct}). Even larger values were found in the case of pristine Li electrode (532.7 Ω for R_{SEI} and 173 Ω for R_{ct}). After 50 cycles at the same conditions, the R_{SEI} and R_{ct} of Li {110} decreased to 104.6 and 56.1 Ω, respectively, remaining to be lower than those of Li{100} (161.3 Ω for R_{SEI} and 66.1 Ω for R_{ct}) and pristine Li (252.1 Ω for R_{SEI} and 80 Ω for R_{ct}). The similar bulk resistance suggests little effect of surface texturing on the conductivity of the metal foils.[43] The decrease observed in both R_{ct} and R_{SEI} for all samples may result from increased Li surface area as well as the formation of SEI with higher ionic conductivity along with cycling, especially for Li{100} and pristine sample. As the Li {110} was found to have smoother surface with cycling, the lowest R_{ct} and R_{SEI} values obtained in the Li {110} electrode then suggested formation of more desirable SEI on the Li {110}. The exchange current density was estimated by fitting the linear region of the Tafel plots (Figure 2d, and Figure S10c,d). A higher exchange current density would suggest easier depositing/stripping of Li.[44] As shown in Figure 2D, Li {110} showed a slightly higher exchange current density (1.12 mA/cm^2) than that of Li {100} (0.57 mA/cm^2) and pristine Li (0.86 mA/cm^2) at the 1st cycle. After 50 cycles, the difference become significant, that is, Li {110} still had the highest exchange current density of 4.52 mA/cm^2, followed by Li {100} (1.77 mA/cm^2) and pristine Li (1.61 mA/cm^2). The observation that the exchange current density increases along with cycling also agrees with the EIS results.

Li//$LiFePO_4$ (Li//LFP) full cells were tested to evaluate the effect of Li foil texturing in a full cell configuration with LFP mass loading of 8.0 mg/cm^2 with a capacity of ~1.5 mAh/cm^2. After being pre-activated at 0.1 C, the cell with Li {100} anode reached a discharge capacity of 135.7 mAh/g and the capacity retention of the corresponding full cell was 36.7% (49.8 mAh/g) after 250 cycles at 1 C (Figure 2E). In the case of Li {110} anode, despite of a slightly lower initial discharge capacity of 130.1 mAh/g, the corresponding full cell showed significantly improved capacity retention of 96.1% (125.0 mAh/g) after 400 cycles at 1C. The Li //LFP full cells made of either Li {100} or {110} anode showed improved capacity retention when compared to cells made of pristine Li foil (without preferential surface texturing). Being similar to results obtained in the symmetrical cells, the electrochemical performance of the full cell with pristine Li foil anode varied. Two examples of a "short-lived" (~20% capacity retention after 250 cycles) and a "long-lived" (~20% capacity retention after 350 cycles) cases are shown in Figure S11, while their initial discharge capacity were always similar (~140 mAh/g). The rate capacities of the full cells at current densities of 0.1, 0.2, 0.5, 1, 2, and 5 C were shown in Figure 2F, and capacity decay at large current density was found in both Li {110} and {100} anode. The difference in the capacity retention between cells adopting Li {110} or {100} electrode was compared in Figure 2G, when a better capacity retention was maintained in the case of Li {110}, and the difference between the two increased toward larger current density. Full cell performance also was tested at a high rate of 5 C. Full cell with Li {110} electrode showed an initial capacity of 103.4 mAh/g, with 94.9% retention (98.2 mAh/g) at the end of 500 cycles, and 81.3% retention (84.1 mAh/g) at the end of 800 cycles, being much superior to those made of Li {100} electrode (Figure S12). At a lower rate of 1 C, the voltage hysteresis (Figure S13) of cells with Li {100} and {110} is similar, with that of Li {110} being slightly lower than Li {110}. The difference became larger for cells cycled at 5 C (0.623 V of Li {110} vs. 0.744 V of Li {110}).

2.4 | Surface composition of cycled samples

The surface composition of all electrodes (Li {110}, {100}, and pristine Li foil) was analyzed by XPS after the 1st cycle (cell cycled at a current density of 1 mA/cm^2 and with a capacity of 1 mAh/cm^2). All samples were washed by DEC to remove residual electrolyte. Compositional analysis suggested the presence of P and F in addition to Li, C, and O (Figure S14), which three elements were also presented in the respective Li foil samples before cell assembly (Figure S7). Consistent observation was made when comparing the fine scans of Li, C, and O in the cycled samples (Figure S14a–c) to those in the as-prepared Li foils (Figure S6a–c). New peaks at ~54.9, 56.0, and ~58.5 eV in the Li 1s (Figure S14a) spectra suggested the formation of $ROCO_2LI$, LiF, and $Li_xPO_yF_z$,[45–47] in addition to the original Li_2O and Li_2CO_3. Similarly, new peaks fitted at ~284.2 and ~285.7 eV in the C 1s spectra suggested the presence of C—F and $ROCO_2LI$ (Figure S14b).[47,48] In the O 1s scan (Figure S14c), new components with binding energy at ~533.0, ~533.8, and ~540.0 eV consistently revealed the presence of $ROCO_2Li$, phosphate, and $Li_xPO_yF_z$[46,49,50] in the surface composition of the cycled Li foil samples. The 1s spectra of F in all samples (Figure S14d) can be fitted by three peaks at ~684.9, ~686.6, and ~687.5 eV, agreeing with the binding energies of LiF, F—C, and $Li_xPO_yF_z$.[51-53] Consistent result was found for the P 2p spectra (Figure S14e), that is, the two peaks fitted at ~134.3, and ~136.9 eV matched those of phosphate and $Li_xPO_yF_z$.[54,55] The XPS results from all Li foil samples after the 1st cycle suggest a modified surface composition due to the

formation of solid electrolyte interphase (SEI). The F and P elements came from the $LiPF_6$ decomposition upon cycling. The changed chemical states of both P and F suggested their participation in the new phase formation in SEI. It is interesting to note that the relatively high-atomic ratios of Li (19.95%), F (12.77%), and P (1.64%) are found in the surface composition of the pristine Li foil after cycling, when compared to the two other samples

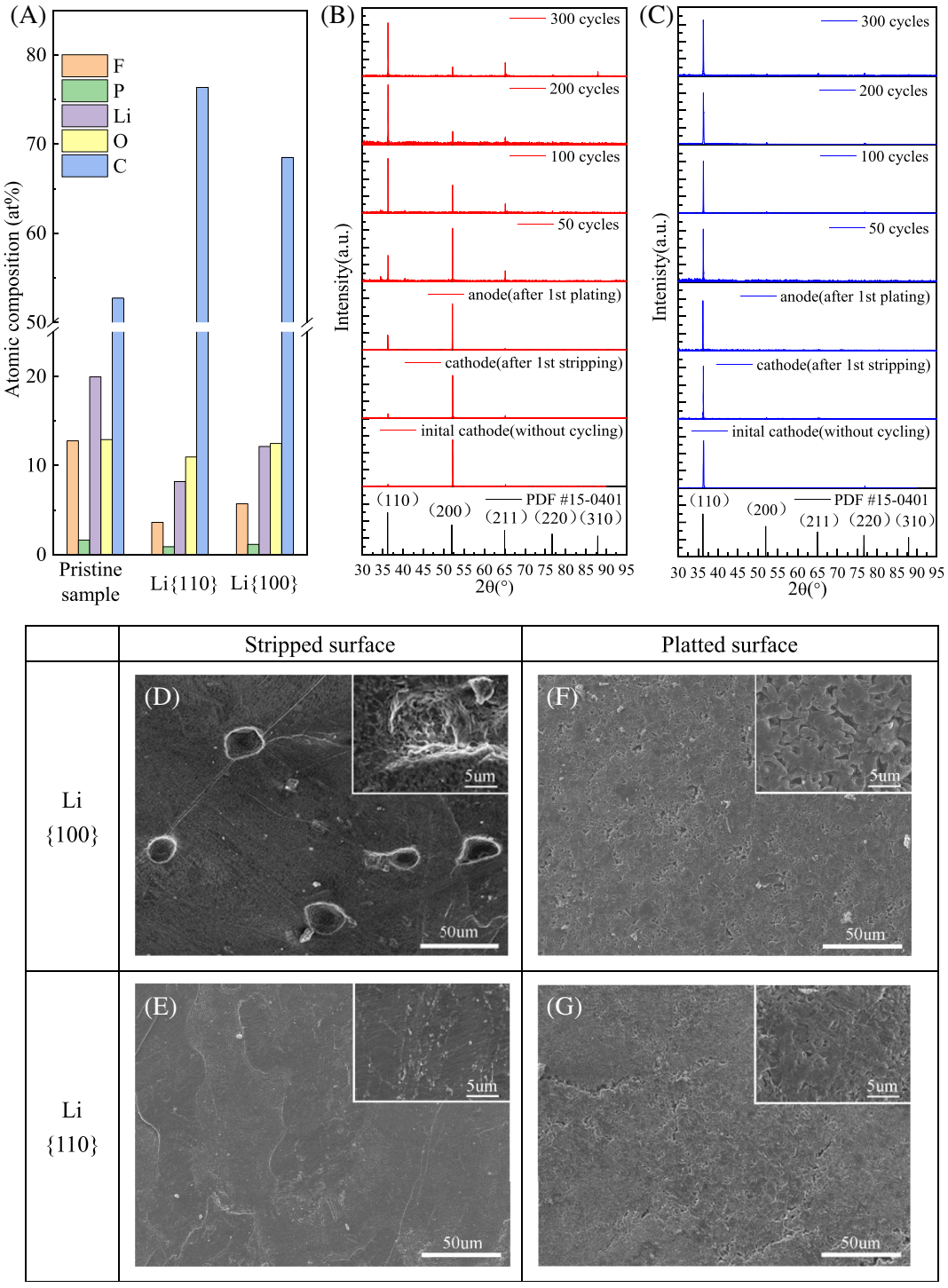

FIGURE 3 (A) The composition comparison among the three samples of pristine Li, Li {110}, and Li {100} foil electrodes after the 1st cycle (cell cycled at a current density of 1 mA/cm^2 and with a capacity of 1 mAh/cm^2). The evolution of XRD patterns of the symmetrical cells with (B) Li {100} and (C) Li {110} electrode cycled at a current density of 1 mA/cm^2 with a capacity of 1mAh/cm^2. (D) Li {100} and (E) Li {110} surface morphology after being stripped at a current density of 1 mA/cm^2 with a capacity of 1mAh/cm^2. (F) Li {100} and (G) Li {110} surface morphology after being platted at a current density of 1 mA/cm^2 with the capacity of 1 mAh/cm^2

(Figure 3A). The fine scan of the respective elements also revealed the relatively high ratios of LiF in the same sample.

2.5 | Texturing and morphology evolution during cycling

Texturing evolution of the Li {110} and {100} electrode was investigated by ex situ XRD taken at different cycle numbers. The symmetrical cells were cycled at a current density of 1 mA/cm^2 with a capacity of 1 mAh/cm^2. After being firstly charged to the capacity of 1 mAh/cm^2, the cathode of the symmetrical cells using Li {100} experienced a stripping process. As shown in Figure 3B, the signal of the (110) diffraction that was nearly absent in the initial cathode (without cycling) remains insignificant. At the same time, signal of the (110) diffraction was found in the anode that experienced plating. At the end of the 50th cycle, the (200) diffraction remained to be the strongest one, but the intensity of the (110) diffraction was found to grow continuously with cycles. At the end of the 100th cycle, the (110) diffraction became the dominant one, outgrowing the (200) diffraction. It is interesting to note that at the end of the 300th cycle, the diffraction intensity of (211) also outgrew that of the (200). In contrast, the diffraction intensity of (110) maintained its dominance in the case of Li {110} electrode from the 1st to the last cycles. Little diffraction intensity of (211) or (200) can be observed even after 300th cycle (Figure 3C).

When symmetrical cells were cycled at a current density of 5 mA/cm^2 with the same capacity (1 mAh/cm^2), evolution of the XRD patterns of the Li electrode composed of Li {100} or Li {110} foils are shown in Figure S15. After being charged to the capacity of 1 mAh/cm^2, the Li {100} electrode soon loses its preferential texturing of (200), and the (110) diffraction becomes dominant after 50 cycles (Figure S15a). The intensity of the (211) diffraction drastically increases from the 50th to the 100th cycle, and becomes the dominant one at the end of the 100th cycles. In contrast, the diffraction intensity of (110) maintained its dominance in the case of Li {110} electrode to the 100th cycle (Figure S15b). While the Li {100} electrode shorted after the 100th cycle, the Li {110} ran longer. At larger cycle numbers (~150 cycles), low intensity (211), and (200) diffractions become visible in Li {110} electrode (Figure S16). A quantitative comparison of texturing evolution of the respective samples can be found in the Supplementary information (Figure S17). Both of Li{100} and Li{110} tend to end up with the {110} texturing (Figure S17a,b) when being cycled at low rate (This is also true for pristine Li foils). In contrast, even the Li {110} tends to lose its preferential texturing eventually when cycled at a high rate (Figure S17c,d), suggesting competition between thermodynamic and kinetic factors in determining the electrochemical stripping/plating characteristics of Li.

The surface morphologies of the Li {100} and {110} electrodes were also monitored along with cycling. We first compare the stripped surface of Li foils of different texturing in the first cycle.[56] Pitted surface is always found on Li {100} electrode at both current densities of 1 and 5 mA/cm^2, as shown in Figure 3D and Figure S13a. Denser pits appear in samples cycled at 5 mA/cm^2 when compared to those cycled at 1 mA/cm^2. Enlarged images of the pitted regions disclose the porous-like surface inside the pit (inset of Figure 3D and Figure S18a). Similar results are obtained for Li foils without preferential texturing (pristine sample, Figure S19). As a comparison, the stripped surface of Li {110} electrode is very different. At a low-current density of 1 mA/cm^2, the Li surface remains flat with little pit found (Figure 3E). At a higher current density of 5 mA/cm^2, a few pits appear but with size significantly smaller and coverage much lower than those on Li {100} surface (Figure S18b).

At the same time, the Li anode surface is plated. Particle-like deposits formed on the surface of both Li {100} and Li {110} (Figure 3F,G, and Figure S18c,d). For anode made of Li {100}, the plated particle layer at a current density of 1 mA/cm^2 (Figure 3F) appears denser than that at 5 mA/cm^2 (Figure S18c). This trend is also observed in anode made of Li {110} (Figure 3G and Figure S18d). Nonetheless, the plated Li layer is found to be always denser on Li {110} than that on Li {100} at both current densities examined.

In the discharge process followed (first cycle), the plated Li anode is stripped. Similar surface morphologies (significantly pitted surface of Li {100} but not Li {110}) are observed when compared to the Li cathode surface at the end of the first charging processing (Figure S20). The discharge process also results in plating of the Li cathode that is stripped during the initial charging. Most of the pitted surface of Li {100} is covered by the new deposits. A denser surface is always found in the cathode of Li {110} in comparison with Li {100} (Figure S21).

The morphology of Li foils after different number of cycles at a current density of 1 mA/cm^2 with the capacity of 1 mAh/cm^2 are shown in Figure S22. Compared to surface morphology of the Li {100} that was cycled for 50 runs (Figure S22a), the same surface became much rougher when the cycle number was increased to 300 (Figure S22b). In contrast, no obvious deterioration is observed in the surface roughness of the Li {110} until 300 cycles (Figure S22c, d). When the current density was increased to 5 mA/cm^2, the surface morphology evolution of the Li foils is accelerated (compared to those at a low-current density of

1 mA/cm^2) for the Li {100} samples. Obvious surface roughening appeared at 50 cycles for Li {100}, and continued to deteriorate toward longer cycles (Figure S23a-c). In contrast, surface smoothness was maintained for Li {110} with the same number of cycling (Figure S23d-f). Both surface characterization of the Li {110} electrode (SEM results showing the surface smoothness) and its electrochemical performance (absence of internal short circuit features and continuous increase of overpotential in the galvanostatic charge/discharge cycles) suggested that Li dendrite induced internal short circuit is not the major failure mechanism of Li {110}. The unstable electrode/electrolyte interface and consumption of electrolyte are likely to cause the final failure of the device.

2.6 | Theoretical understanding of the plating/stripping characteristics of lithium foils

According to Hagopian et al., Li {110} surface is thermodynamically more stable than Li{100} surface in the electrochemical environment of lithium metal batteries with ethylene carbonate-based electrolyte, which explained our experimental observations that the Li{100} surface will gradually change to Li{110} surface upon repeated stripping and plating.[21] To understand the plating/stripping phenomena of Li on Li foils of specific texturing, slab models of lithium {100} and {110} surfaces with 10–15 Å vacuum layers were constructed and optimized using density functional theory (DFT) calculations. For each surface, two kinds of surface morphology were considered. In one slab model, half layer of the lithium atoms at the surface were removed (labeled as "R_{plane}"), while in the other slab model, the same number of lithium atoms with a cone shape were removed (labeled as "R_{cone}"). The detailed atomic geometries can be found in Figure S24. Afterwards, these surfaces went through 2 ps ab initio molecular dynamics (AIMD) simulations in NVT ensemble. The trajectories of lithium atoms as well as the potential energies were recorded.

After the 2 ps AIMD simulations, as shown in Figure S25, the surfaces with "R_{plane}" morphology show little difference, while for the surfaces with "R_{cone}" morphology, the "nano pit" were somehow filled by neighboring Li atoms. For Li {100} surface, the "nano pit" becomes a bit shallower, while for Li {110} surface, the "nano pit" nearly disappeared. To quantitively describe this phenomenon, we tracked the mean height of the initially exposed surface Li atoms in the "R_{cone}" cases of both Li {100} and Li {110} as shown in Figure 4A,B. When the "nano pit" is filled by neighboring Li atoms, the mean height of exposed surface Li atoms will decrease as illustrated in Figure S26. It can be found that for Li {100} surface, the mean height of the initially exposed surface atoms fluctuates around a certain value, indicating that the "nanopit" remains during the simulation. While for the Li {110} case, the mean height of initially exposed surface atoms decreased about 0.5 Å, indicating that neighboring Li atoms filled the "nano pit" during the simulation.

These results agree well with previous report that the surface diffusion energy barrier of Li atom on Li {110} surface is only about one half of that of Li {100} surface, which will result in better surface diffusivity.[20] We also compared the potential energy of "R_{cone}" and "R_{plane}" cases for both Li {100} and Li {110} surface as shown in Figure 4C,D. For both cases, the "R_{plane}" case shows a lower potential energy compared with the "R_{cone}" case. For the Li {100} surface, the initial energy difference between these two cases is small, and the energy difference fluctuated around 0.02 Ha during the entire simulation. While for the Li {110} surface, the energy difference between these two cases is much larger. As the simulation went on, the "nano pit" will be gradually filled by the neighboring Li atoms and the energy difference gradually decreased to zero. This potential energy analysis suggests in addition to the kinetic reason that Li {110} surface shows a smaller diffusion energy barrier, the "R_{cone}" morphology in Li {100} is also thermodynamically more stable than that in the Li {110} case. Therefore, during the lithium stripping process, Li {100} surface tends to preserve a rough surface morphology when "nano pits" were formed; while for Li {110} surface, once a "nano pit" was created, it will be soon filled by neighboring Li atoms and result in a much smoother surface morphology, which agree well with our experimental observations. A flat and thus dense Li {110} surface is both thermodynamically and kinetically preferred upon cycling, and consequently the significantly reduced inhomogeneity of Li plating/stripping associated with Li {110} texturing contributes to the improved electrode cycle stability. Schematic illustration of plating/stripping characteristic of the Li{100} and Li{110} is shown in Figure 4E,F, respectively.

3 | CONCLUSION

Li metal electrode with {110} texturing is demonstrated to have significantly improved cycle stability in both devices adopting symmetrical cell and full cell configurations, when compared to the same Li metal electrode with {100} texturing or without any specific texturing (pristine Li foil). Even without any artificial SEI introduced in the present work, the Li {110} electrode showed comparable performance to those with artificial SEI in the literature. Being different from Li {100} or pristine Li foil, Li metal electrode with {110} texturing is found to maintain both

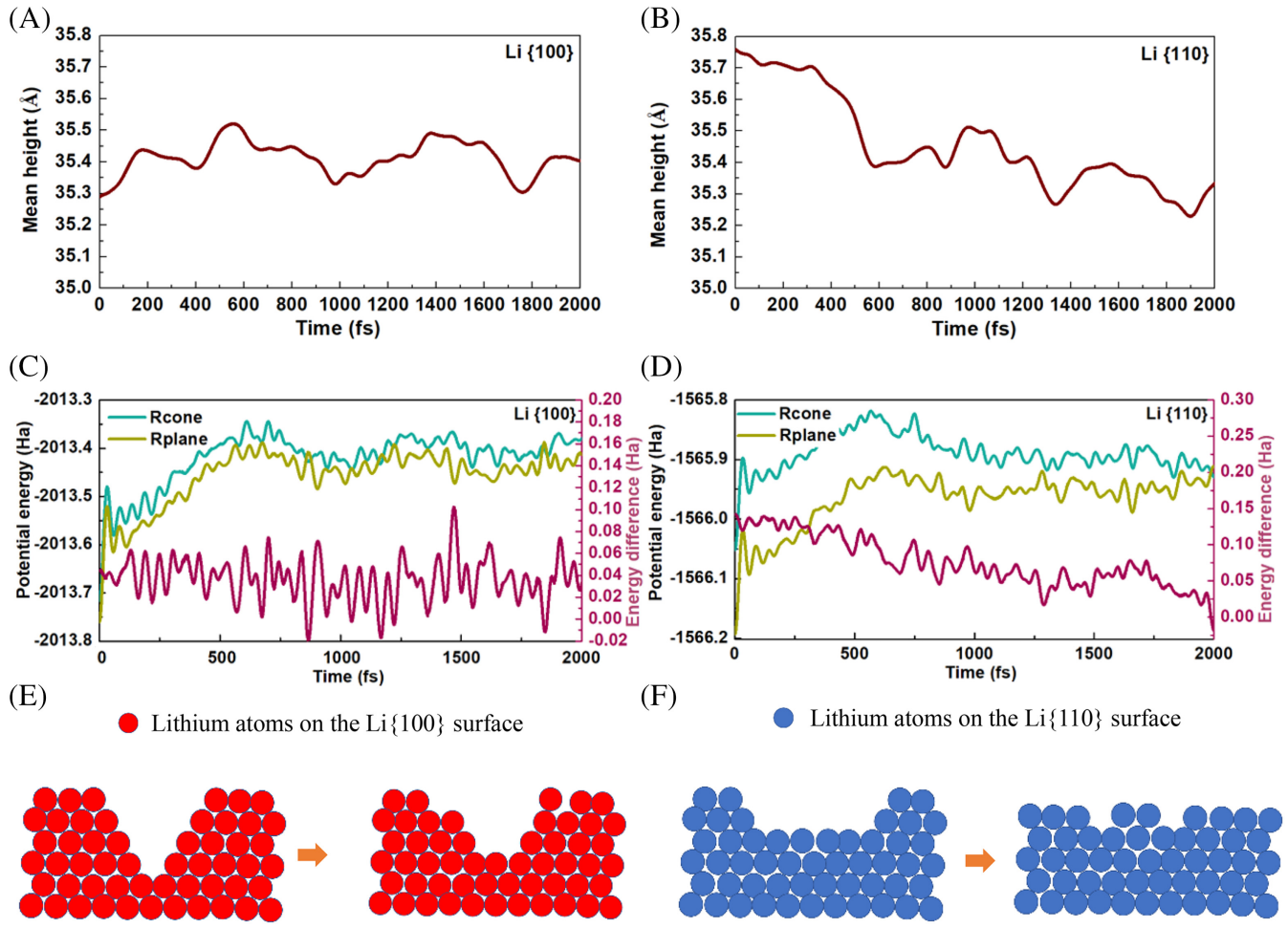

FIGURE 4 Mean height (gray line) and its deviation (gray area) of exposed surface atoms in "R_{cone}" case as a function of simulation time for (A) Li {100} surface, and (B) Li {110} surface. Potential energy as a function of simulation time for (C) Li {100} surface, and (D) Li {110} surface with different initial morphology. Schematic illustration of plating/stripping characteristics of (E) Li {100} and (F) Li {110}

the {110} preferential crystallographic orientation and the surface flatness upon repeated cycling even at a large current density of 5 mA/cm^2. The significantly enhanced cycling performance of Li {110} is ascribed to the uniform stripping and dense plating of Li on the Li {110} surface upon cycling, due to the low-surface energy and surface diffusion barrier associated with such a plane in an electrochemical environment. Experimental results also suggest that the Li {110} also associate with more efficient charge transfer in cycling.

4 | METHOD

4.1 | Chemical polishing of Li foil electrodes

All Li foils were chemically polished first using a tetrahydrofuran solution of Naphthalene (0.192 g Naphthalene crystal) (>99.5%, Sigma-Aldrich) dissolved in 15 ml anhydrous tetrahydrofuran (>99.8%, Sigma-Aldrich) for 2 min.[2] After that the Li foils were rinsed by diethyl carbonate (DEC) (>99.8%, Sigma-Aldrich) for a few times to remove the polishing chemicals. All procedures were carried out in a glove box with oxygen and water content below 0.5 ppm.

4.2 | Texture formation of Li metal foil

To prepare Li foils of {110} texturing, the pristine Li foil (China Energy Lithium Co., LTD) was pre-rolled at room temperature using a stainless steel shaft. The surface of Li foil was then scraped in a uni-directional manner. After that, the lithium foil was further rolled using the same stainless steel shaft at 75°C. Such a sample is denoted as Li {110}.

To prepare Li foils of {100} surface crystallographic orientation, a pristine Li foil of the same size was pressed at 5 MPa for a few seconds by a hydraulic press at room temperature. Such a sample is denoted as Li {100}.

4.3 | Measurements of performance of symmetric cells

CR-2032-type coin cells were assembled to investigate the electrochemical performance of Li foil with specific texturing. Symmetric cells were prepared using lithium foils with the same surface crystallographic orientation (i.e., {100} or {110}). 1M lithium hexafluorophosphate ($LiPF_6$) (anhydrous, Sigma-Aldrich) in 1:1 ethylene carbonate (EC) (>99.8%, Sigma-Aldrich)/diethyl carbonate (DEC) were adopted as the electrolyte. A series of symmetrical cells were assembled and cycled at current densities of 1, 2, and 5 mA/cm^2 with a capacity of 1 mAh/cm^2. At different cycle numbers, the cells were stopped and disassembled. The disassembled electrodes were rinsed by DEC for a few times to remove the electrolyte. Then they were sent to ex-situ XRD experiments for investigation of crystallographic evolution, or transferred to the scanning electron microscope (SEM) for surface morphology inspection of the Li foils along with cycling.

4.4 | Measurements of performances of Li||$LiFePO_4$ batteries

Standard CR2032 coin-type cell were also employed for the assembly of Li//$LiFePO_4$ (LFP) full cells. The electrolyte used for full cell was 1.0 M $LiPF_6$ in EC/DEC (v/v = 1:1). Sixty microliters liquid electrolyte was used in full cell test. The cathode was prepared by mixing the LFP active material (Sigma-Aldrich), carbon black (TIMCAL) and polyvinylidene fluoride (PVDF) (Arkema) at the weight ratio of 8:1:1 in anhydrous *N*-methyl-2-pyrrolidone (NMP) (>99.5%,Macklin), and casting the formed slurry on the aluminum foil with LFP mass loading of and 8.0 mg in the cathode. The cells were precycled at 0.1 C for three rounds to activate the cathode. After that, they were cycled at 1, 2, and 5 C in a voltage range of 2.2–4.0 V verse Li^+/Li.[57]

4.5 | Characterizations

In order to estimate the grain size on the surface, the samples were immersed in an etching solution (1.92 g Naphthalene crystal (>99.5%, Sigma-Aldrich) dissolved in 15 ml anhydrous tetrahydrofuran (>99.8%, Sigma-Aldrich)) for 30s to disclose the grain boundaries. The samples are then cleaned several times with diethyl carbonate. Galvanostatic cycling and full cell performance were examined on LANHE CT2001A battery testing system (LAND Electronics). The XRD test was conducted on a Rigaku SmartLab diffractometer (Cu Kα radiation) at 40 kV, 40 mA with scan rate of 5° min^{-1} and a testing area of $10 \times 10\ mm^2$.The sample was loaded onto a special holder with a Kapton window in the glove box. SEM images were taken with an JSM 7800F scanning electron microscope at an acceleration voltage of 5 kV. The samples were transferred by a homemade vacuum chamber from the glove box to the microscope to avoid exposure to air. Al Ka X-ray line was used by X-ray photoelectron spectrometer (Nexsa). EIS and Tafel measurements for symmetric cells were performed using the CHI 760E electrochemical workstation at room temperature. EIS was tested with a frequency range from 10^{-2} to 10^5 HZ with an amplitude of 5 mV. Tafel measurement was carried out with a voltage ranging from −0.4 to 0.4 V with a scan rate of 1 mV/s.

4.6 | Density functional theory (DFT) calculations

Density functional theory (DFT) calculations were performed using abinit software package.[58–60] Perdew–Burke–Ernzerhof (PBE) generalized gradient approximation (GGA) and projector augmented wave (PAW)[61,62] pseudopotentials were employed to treat the exchange-correlation functionals and electron-ion interactions. The cut-off energy was set to be 20 Ha, and the *k*-point mesh was set to be less than 0.05 $Å^{-1}$.

Ab initio molecular dynamics (AIMD) simulations were performed using Cp2K software package.[63] In NVT ensemble, Nośe–Hoover chains thermostat with a time constant of 100 fs was used to keep the temperature at $T = 300$ K. Born-Oppenheimer MD was used for the propagation of classical nuclei.[64] The convergence criterion was set to be 1×10^{-7} a.u. for the optimization of the wave function using the Gaussian and plane waves method. The wave function was expanded in the Gaussian double zeta with valence polarization functions (DZVP) basis set. An auxiliary basis set of plane waves was used to expand the electron density up to a cutoff of 400 Ry. The core electrons were treated using PBE gradient correction and Geodecker–Teter–Hutter pseudopotentials. A time step of 0.5 fs was adopted for all the simulations.[61,65]

ACKNOWLEDGMENTS

QL acknowledged the support from CUHK direct grant under project no. 4053530.

CONFLICT OF INTEREST

The authors declare no conflict of interest.

ORCID

Xitao Hu https://orcid.org/0000-0002-2543-445X
Yao Gao https://orcid.org/0000-0001-8308-4729
Biao Zhang https://orcid.org/0000-0001-8687-8946
Le Shi https://orcid.org/0000-0003-1468-4549
Quan Li https://orcid.org/0000-0001-8563-1802

REFERENCES

1. Li L, Basu S, Wang Y, et al. Self-heating–induced healing of lithium dendrites. *Science*. 2018;359(6383):1513-1516.
2. Tang W, Yin X, Chen Z, Fu W, Loh KP, Zheng GW. Chemically polished lithium metal anode for high energy lithium metal batteries. *Energy Storage Mater*. 2018;14:289-296.
3. Huo H, Chen Y, Li R, et al. Design of a mixed conductive garnet/Li interface for dendrite-free solid lithium metal batteries. *Energ Environ Sci*. 2020;13(1):127-134.
4. Yu S, Schmidt RD, Garcia-Mendez R, et al. Elastic properties of the solid electrolyte $Li_7La_3Zr_2O_{12}$ (LLZO). *Chem Mater*. 2016; 28(1):197-206.
5. Xu C, Ahmad Z, Aryanfar A, Viswanathan V, Greer JR. Enhanced strength and temperature dependence of mechanical properties of Li at small scales and its implications for Li metal anodes. *Proc Natl Acad Sci U S A*. 2017;114(1):57-61.
6. Ke X, Liang Y, Ou L, et al. Surface engineering of commercial Ni foams for stable Li metal anodes. *Energy Storage Mater*. 2019;23:547-555.
7. Kim YJ, Kwon SH, Noh H, et al. Facet selectivity of cu current collector for Li electrodeposition. *Energy Storage Mater*. 2019; 19:p154-p162.
8. Fan L, Zhuang HL, Gao L, Lu Y, Archer LA. Regulating Li deposition at artificial solid electrolyte interphases. *J Mater Chem A*. 2017;7(7):3483-3492.
9. Lin D, Liu Y, Chen W, et al. Conformal lithium fluoride protection layer on three-dimensional lithium by nonhazardous gaseous reagent freon. *Nano Lett*. 2017;17(6):3731-3737.
10. Sun Y, Zhao Y, Wang J, et al. A novel organic "Polyurea" thin film for ultralong-life lithium-metal anodes via molecular-layer deposition. *Adv Mater*. 2019;31(4):1806541.
11. Coblas SG, Fatu A, Maoui A, et al. Manufacturing textured surfaces: state of art and recent developments. *Proc Inst Mech Eng J*. 2015;229(1):3-29.
12. Zheng J, Deng Y, Yin J, et al. Textured electrodes: manipulating built-in crystallographic heterogeneity of metal electrodes via severe plastic deformation. *Adv Mater*. 2021;2106867(1):2106867.
13. Zhou M, Guo S, Li J, et al. Surface-preferred crystal plane for a stable and reversible zinc anode. *Adv Mater*. 2021;33(21):2100187.
14. Wang X, Meng J, Lin X, et al. Stable zinc metal anodes with textured crystal faces and functional zinc compound coatings. *Adv Funct Mater*. 2021;31(48):2106114.
15. Shi F, Pei A, Vailionis A, et al. Strong texturing of lithium metal in batteries. *Proc Natl Acad Sci U S A*. 2017;114(46): 12138-12143.
16. Li Y, Li Y, Pei A, et al. Atomic structure of sensitive battery materials and interfaces revealed by cryo–electron microscopy. *Science*. 2017;358(6362):506-510.
17. Gu Y, Xu HY, Zhang XG, et al. Lithiophilic faceted cu (100) surfaces: high utilization of host surface and cavities for lithium metal anodes. *Angew Chem Int Ed*. 2019;58(10):3092-3096.
18. Zhao Q, Deng Y, Utomo NW, et al. On the crystallography and reversibility of lithium electrodeposits at ultrahigh capacity. *Nat Commun*. 2021;12(1):1-10.
19. Zheng Y, Soto FA, Ponce V, et al. Localized high concentration electrolyte behavior near a lithium–metal anode surface. *J Mater Chem A*. 2019;7(43):25047-25055.
20. Shi L, Xu A, Zhao T. First-principles investigations of the working mechanism of 2D h-BN as an interfacial layer for the anode of lithium metal batteries. *ACS Appl Mater Interfaces*. 2017; 9(2):1987-1994.
21. Hagopian A, Marie D, Jean F. Thermodynamic origin of dendrite growth in metal anode batteries. *Energ Environ Sci*. 2020; 13(12):5186-5197.
22. Al-Salehi F, Lancaster P. An experimental determination of the roll pressure distributions in cold rolling. *Int J Mech Sci*. 1973; 15(9):693-710.
23. Robert G, Matthias M, Gunter G. Texture effects on plastic deformation of magnesium. *Mater Sci Eng A*. 2005;395(1-2):338-349.
24. Van P. Simulation of the rolling and shear texture of brass by the Taylor theory adapted for mechanical twinning. *Acta Metall*. 1978;26(4):591-604.
25. Hayakawa Y, Szpunar J. A new model of Goss texture development during secondary recrystallization of electrical steel. *Acta Mater*. 1997;45(11):4713-4720.
26. Yao K, Kwabi D, Quinlan R, et al. Thermal stability of Li_2O_2 and Li_2O for Li-air batteries: in situ XRD and XPS studies. *J Electrochem Soc*. 2013;160(6):824-830.
27. Vardar G, Bowman WJ, Lu Q, et al. Structure, chemistry, and charge transfer resistance of the Interface between $Li_7La_3Zr_2O_{12}$ electrolyte and $LiCoO_2$ cathode. *Chem Mater*. 2018;30(18):6259-6276.
28. Huo H, Chen Y, Zhao N, et al. In-situ formed Li_2CO_3-free garnet/Li interface by rapid acid treatment for dendrite-free solid-state batteries. *Nano Energy*. 2019;61:119-125.
29. Lu M, Cheng H, Yang Y. A comparison of solid electrolyte interphase (SEI) on the artificial graphite anode of the aged and cycled commercial lithium ion cells. *Electrochim Acta*. 2008;53(9):3539-3546.
30. Howlett P, Brack N, Hollenkamp A, Forsyth M, MacFarlane D. Characterization of the lithium surface in N-methyl-N-alkylpyrrolidinium bis(trifluoromethanesulfonyl)amide room temperature ionic liquid electrolytes. *J Electrochem Soc*. 2006;153(3): 595-606.
31. Becking J, Gorbmeyer A, Kolek M, et al. Lithium-metal foil surface modification: an effective method to improve the cycling performance of lithium-metal batteries. *Adv Mater Interfaces*. 2017;4(16):1700166.
32. Hornsveld N, Put B, Kessels WMM, Vereecken PM, Creatore M. Plasma-assisted and thermal atomic layer deposition of electrochemically active Li_2CO_3. *RSC Adv*. 2017;7(66):41359-41368.
33. Benseddik E, Makhlouki M, Bernede JC, Lefrant S, Proń A. XPS studies of environmental stability of polypyrrole-poly(vinylalcohol) composites. *Synth Met*. 1995;72(3):237-242.
34. Wang L, Menakath A, Han F, et al. Identifying the components of the solid–electrolyte interphase in Li-ion batteries. *Nat Chem*. 2019; 11(9):789-796.

35. Guo W, Liu S, Guan X, Zhang X, Liu X, Luo J. Mixed ion and electron-conducting scaffolds for high-rate. *Adv Energy Mater*. 2019;9(20):1900193.
36. Qin L, Wang K, Xu H, et al. The role of mechanical pressure on dendritic surface toward stable lithium metal anode. *Nano Energy*. 2020;77:105098.
37. Gu Y, Wang WW, Li YJ, et al. Designable ultra-smooth ultra-thin solid-electrolyte interphases of three alkali metal anodes. *Nat Commun*. 2018;9(1):1339.
38. Zheng G, Xiang Y, Chen S, et al. Additives synergy for stable interface formation on rechargeable lithium metal anodes. *Energy Storage Mater*. 2020;29:77-385.
39. Zhang P, Yuan T, Pang T, et al. Influence of current density on graphite anode failure in lithium-ion batteries. *J Am Chem Soc*. 2019;166:A5489.
40. Jiao S, Zheng J, Li Q, et al. Behavior of lithium metal anodes under various capacity utilization and high current density in lithium metal batteries. *Joule*. 2018;2(1):110-124.
41. Shen X, Li Y, Qian T, et al. Lithium anode stable in air for low-cost fabrication of a dendrite-free lithium battery. *Nat Commun*. 2019;10(1):1-9.
42. Yu L, Chen S, Lee H, et al. A localized high-concentration electrolyte with optimized solvents and lithium difluoro (oxalate) borate additive for stable lithium metal batteries. *ACS Energy Lett*. 2018;3(9):2059-2067.
43. Jadhav S, Dadbakhsh S, Goossens L, et al. Influence of selective laser melting process parameters on texture evolution in pure copper. *J Mater Process Technol*. 2019;270:47-58.
44. Wang H, Liu M, Wang X, et al. A self-smoothing Li-metal anode enabled via a hybrid interface film. *J Mater Chem A*. 2020;8(24):12045-12054.
45. Yan C, Yao YX, Chen X, et al. Lithium nitrate solvation chemistry in carbonate electrolyte sustains high-voltage lithium metal batteries. *Angew Chem*. 2018;130(43):14251-14255.
46. Kuwata H, Sonoki H, Matsui M, Matsuda Y, Imanisi N. Surface layer and morphology of lithium metal electrodes. *Electrochemistry (Tokyo)*. 2016;84(11):854-860.
47. Palchan I, Cerspin M, Estrade-Szwarckopf H, Rousseau B. Graphite fluorides: an Xps study of a new type of a new type of C-F bonding. *Chem Phys Lett*. 1989;4:321-327.
48. Yan C, Cheng XB, Tian Y, et al. Dual-layered film protected lithium metal anode to enable dendrite-free lithium deposition. *Adv Mater*. 2018;30(25):1707629.
49. Togasaki N, Momma T, Osaka T. Role of the solid electrolyte interphase on a Li metal anode in a dimethylsulfoxide-based electrolyte for a lithium-oxygen battery. *J Power Sources*. 2015;294:588-592.
50. Cao Z, Zhu G, Zhang R, et al. Biological phytic acid guided formation of monodisperse large-sized carbon@$LiFePO_4$/graphene composite microspheres for high-performance lithium-ion battery cathodes. *Chem Eng J*. 2018;351:382-390.
51. Parimalam B, Macintosh A, Kadam R, et al. Decomposition reactions of anode solid electrolyte interphase (SEI) components with $LiPF_6$. *J Phys Chem C*. 2017;121(41):22733-22738.
52. Xiong X, Wang Z, Yin X, Guo H, Li X. A modified LiF coating process to enhance the electrochemical performance characteristics of $LiNi_{0.8}Co_{0.1}Mn_{0.1}O_2$ cathode materials. *Mater Lett*. 2013;110:4-9.
53. Zhang X, Cheng X, Chen X, et al. Fluoroethylene carbonate additives to render uniform Li deposits in lithium metal batteries. *Adv Funct Mater*. 2017;27(10):1605989.
54. Dedryvere R, Martinez H, Leroy S, et al. Surface film formation on electrodes in a $LiCoO_2$/graphite cell: a step by step XPS study. *J Power Sources*. 2007;174(2):462-468.
55. Zheng Y, He YB, Qian K, et al. Deterioration of lithium iron phosphate/graphite power batteries under high-rate discharge cycling. *Electrochim Acta*. 2015;176:270-279.
56. Gireaud L, Grugeon S, Laruelle S, Yrieix B, Tarascon JM. Lithium metal stripping/plating mechanisms studies: a metallurgical approach. *Electrochem Commun*. 2006;8(10):1639-1649.
57. Zaghib K, Mauger A, Gendron F, Julien CM. Relationship between local structure and electrochemical performance of LiFePO 4 in Li-ion batteries. *Ionics*. 2008;14(4):271-278.
58. Gonze X, Beuken JM, Caracas R, et al. First-principles computation of material properties: the ABINIT software project. *Comput Mater Sci*. 2002;25(3):478-492.
59. Gonze X, Amadon B, Anglade PM, et al. ABINIT: first-principles approach to material and nanosystem properties. *Comput Phys Commun*. 2009;180(12):2582-2615.
60. Gonze X. A brief introduction to the ABINIT software package. *Cryst Mater*. 2005;220(5-6):558-562.
61. Perdew JP, Ernzerhof M, Burke K. Rationale for mixing exact exchange with density functional approximations. *J Chem Phys*. 1996;105(22):9982-9985.
62. Blöchl PE. Projector augmented-wave method. *Phys Rev B*. 1994;50(24):17953-17979.
63. VandeVondele J, Krack M, Mohamed F, Parrinello M, Chassaing T, Hutter J. Quickstep: fast and accurate density functional calculations using a mixed Gaussian and plane waves approach. *Comput Phys Commun*. 2005;167(2):103-128.
64. Martyna GJ, Klein ML, Tuckerman M. Nosé–hoover chains: the canonical ensemble via continuous dynamics. *J Chem Phys*. 1992;97(4):2635-2643.
65. Goedecker S, Teter M, Hutter J. Separable dual-space Gaussian pseudopotentials. *Phys Rev B*. 1996;54(3):1703-1710.

SUPPORTING INFORMATION

Additional supporting information can be found online in the Supporting Information section at the end of this article.

How to cite this article: Hu X, Gao Y, Zhang B, Shi L, Li Q. Superior cycle performance of Li metal electrode with {110} surface texturing. *EcoMat*. 2022;4(6):e12264. doi:10.1002/eom2.12264